Chapter 5

Toward atom-photon entanglement

The tools that we have developed over the past few years for control and interrogation of our atom-cavity system have brought us to the point where we can now implement complex protocols in the lab. Our current efforts focus on one such protocol, which would generate entanglement between the polarization states of a photon and the Zeeman states of a trapped atom. In Section 5.1, I describe the details of this entanglement scheme. Section 5.2 discusses the use of Rabi flops to characterize decoherence in our system; an understanding of decoherence mechanisms is necessary in order to determine whether we will be able to demonstrate entanglement. Section 5.3 presents our method for mapping superpositions of Zeeman states to hyperfine states that we have developed in the context of this entanglement project. In order to quantify the coherence of the mapping, we vary the phase between two arms of this process and generate a fringe. Section 5.4 centers on the final step in the protocol: fast pulses from the side of the cavity that excite the atom to the $F' = 5$ manifold. Here I also discuss the current outlook for the project.

5.1 Atom-photon entanglement scheme

The concept of atom-photon entanglement lies at the heart of cavity-QED-based schemes for quantum networking. These schemes rely on entanglement in order to transfer information coherently between long-lived atomic superpositions (quantum nodes) and photonic states in optical fiber (quantum channels). In Chapter 3 of

this thesis, I discuss one such mapping, between cesium hyperfine manifolds $F = 3$ and $F = 4$ and photon Fock states $|0\rangle$ and $|1\rangle$. However, a more robust scheme would entangle the atomic state with photon polarization rather than photon number. Losses in the optical path will inevitably degrade the entangled state: if the original composite system is given by

$$|\psi\rangle = |a_1\rangle \otimes |p_1\rangle + |a_2\rangle \otimes |p_2\rangle, \tag{5.1}$$

where $a_{1,2}$ and $p_{1,2}$ are atom and photon states, then after propagation, the density matrix $\rho = |\psi\rangle\langle\psi|$ becomes

$$\rho' = (1 - p_E)(|a_1\rangle + |a_2\rangle)(\langle a_1| + \langle a_2|) \otimes |0\rangle\langle 0| + p_E|\psi\rangle\langle\psi|, \tag{5.2}$$

where the entanglement probability p_E is determined by path losses and $|0\rangle$ represents the absence of a photon. In the case of the Fock state mapping, if we do not detect a photon at the cavity output, we cannot distinguish whether this corresponds to p_1 (and thus to a_1) or to $|0\rangle$. For polarization states, however, decoupling photon number from entanglement means that we can restrict ourselves to a heralded, effective entangled state $|\psi\rangle\langle\psi|$ with probability p_E [103].

Recent work in Gerhard Rempe's group has shown that it is possible to control photon polarization based on the Zeeman state of an atom within a cavity [82, 83]. A magnetic field along the cavity axis is used to split out the Zeeman levels of ^{87}Rb, and the cavity is tuned into resonance with the $F = 1 \rightarrow F' = 1$ transition between the $5S_{1/2}$ and $5P_{3/2}$ manifolds. For an atom prepared in $|F = 2, m_F = 0\rangle$, an initial STIRAP process driven by a laser on the $F = 2 \rightarrow F' = 1$ transition will either a) transfer the atom to the $|1, -1\rangle$ ground state while generating a cavity photon with σ^+ polarization, or b) transfer the atom to $|1, 1\rangle$ while generating a σ^- photon. A second STIRAP process on the $F = 1 \rightarrow F' = 1$ transition is conditional on the result of the first: a σ^- photon is generated if the atom is in $|1, -1\rangle$, and a σ^+ photon if the atom is in $|1, 1\rangle$. Thus, alternating the two classical laser pulses creates

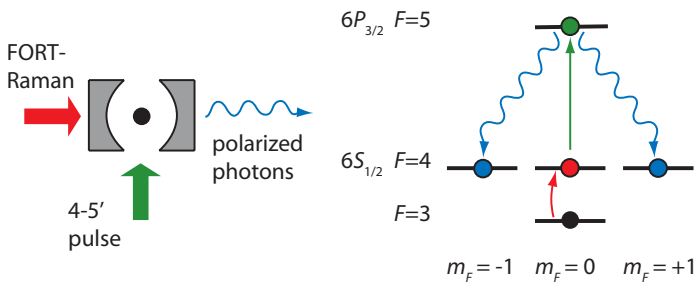

Figure 5.1: Scheme for generating entanglement between the polarization states of a photon and the Zeeman states of a trapped atom. We optially pump a cesium atom to $|3,0\rangle$, then transfer it to $|4,0\rangle$ via a Raman π pulse. A fast pulse from the side of the cavity excites the atom to $|5',0\rangle$. Atomic decay into the cavity mode will generate a circularly polarized photon; a σ^+ photon corresponds to the final atomic state $|4,-1\rangle$, and a σ^- photon corresponds to $|4,1\rangle$.

sequential pairs of polarization-entangled photons, which can be detected in the cavity transmission path [83]. While these experiments represent a significant step towards quantum networking, it is important to note that they were done with atoms falling through the cavity mode. For information storage in quantum nodes, we require photon generation using trapped, localized atoms that could then be re-addressed at later times. In addition, we would like to quantify atom-photon entanglement directly by reading out the atomic state rather than by generating a second photon. As our efficient method of state detection [30] only distinguishes between hyperfine manifolds, we will first have to introduce a mapping between Zeeman and hyperfine states.

We begin our protocol by preparing a single cesium atom in $|4,0\rangle$. (In practice, we use the methods of Chapter 4 to prepare the atom in $|3,0\rangle$, then transfer the population to $|4,0\rangle$ via a Raman π pulse.) As in the Rempe experiment, a magnetic field splits out the Zeeman states, and we define a quantization direction along the magnetic field axis. A ~ 10 ns π-polarized optical pulse from the side of the cavity resonant with the $F = 4 \rightarrow F' = 5$ transition excites the atom. Because the pulse is polarized along the cavity axis, the cavity mode only supports atomic decay to states $|4,1\rangle$ and $|4,-1\rangle$, with σ^- and σ^+ polarization, respectively. Photon polarization is straightforward to detect with waveplates and beamsplitters at the cavity output. To

read out the atomic state, we want to map superpositions of $|4,1\rangle$ and $|4,-1\rangle$ onto $F = 3$ and $F = 4$, as we are able to measure superposition states of the hyperfine manifolds. We apply two simultaneous Raman π pulses tuned to the $|4,1\rangle \rightarrow |3,0\rangle$ and $|4,-1\rangle \rightarrow |3,0\rangle$ transitions, where the $\Delta m = \pm 1$ transitions rely on a component of the magnetic field transverse to the cavity axis; we expect the populations to interfere constructively or destructively depending on the relative phase of the two initial states, so that as a function of phase, the atom will either be transferred to $F = 3$ or remain in $F = 4$.

Section 5.3 presents our efforts to characterize this interference process. First, however, we note that our scheme relies on carefully tuned Raman pulses at three different frequencies, two of which are sensitive to the magnetic field. In the following section, then, we investigate the decoherence mechanisms underlying our Raman technique to understand whether this is feasible.

5.2 Rabi flops

5.2.1 Theory

The Bloch equations describe the evolution of a spin system in an applied field [104]; while these equations were first introduced to describe magnetic resonance phenomena, they also apply to a two-level atom driven by an optical field, or to our current situation, in which two atomic ground states are coupled via Raman transitions. The Rabi solution of the Bloch equations for a resonant driving field shows that population initially prepared in one spin state will be driven coherently back and forth between the two states, a process known as "Rabi flopping." The rate of population transfer is given by the Rabi frequency Ω, which is proportional to the square root of the intensity of the driving field. Specifically, the duration of a "π pulse," that is, the time required to transfer population from one state to the other, is given by

$$t_\pi = \frac{\pi}{\Omega}. \tag{5.3}$$

For a driving field detuned from resonance by Δ, the population transfer as a function of time is given by the equation

$$P(t) = \frac{\Omega^2}{\Omega^2 + \Delta^2} \sin^2 \sqrt{\Omega^2 + \Delta^2} t/2 \tag{5.4}$$

where $P(t)$ corresponds to the fraction of the population transferred from the initial to the final spin state. Thus in the off-resonant case, the oscillation frequency is faster, but complete inversion between the two states is never achieved.

A more realistic model incorporates phenomenological decay processes into the Bloch equations [104]. The result is that Rabi oscillations are exponentially damped according to a set of characteristic decay times. Conversely, in order to study the decoherence mechanisms within an experiment, one simple technique is to measure Rabi flopping amplitudes and damping rates. In particular, Rabi flops have become an important benchmark for the quantum computing community, as the number of sequential gates that a quantum computer could perform is limited by the ratio of the decay time to t_π.

Several processes contribute to spin decoherence. In the notation used by the nuclear magnetic resonance (NMR) community, the longitudinal decay time T_1 describes population relaxation to thermal equilibrium; T_1 decay is due to spin-lattice coupling in NMR, but in our experiments it is negligible. Meanwhile, the transverse decay time T_2 can be decomposed into two components,

$$\frac{1}{T_2} = \frac{1}{T_2'} + \frac{1}{T_2^*}. \tag{5.5}$$

Here T_2' describes homogeneous, incoherent processes, and T_2^* describes inhomogeneous effects. Note that often when we think of homogeneous and inhomogeneous processes, we imagine a macroscopic ensemble, such as a collection of spins in a crystal or an atom cloud. Homogeneous effects such as collisions would effect all spins identically, while inhomogeneous effects would assign a different value of some property to each spin, such as velocity in the case of Doppler broadening. Here we are dealing

with one atom at a time within a cavity, but the ensemble picture is valid because we collect data over a series of hundreds or thousands of atoms, and we repeat a measurement hundreds of times for each atom. In this case, inhomogeneous T_2^* mechanisms may result from changes over time: for example, variation in the intensity of the Raman beams, or gradual heating of the atoms throughout the Raman process, both of which would effectively assign a different Raman frequency to each flopping measurement. Another potential T_2^* mechanism is the finite temperature of each atom within the FORT, resulting in a periodic modulation of the Rabi frequency. (Because the intensities of both FORT and Raman beams have a Gaussian profile, the Rabi frequency seen by the atoms is spatially dependent.) For field-sensitive transitions, drifts in the magnetic field over time would result in a range of possible detunings from Raman resonance. Meanwhile, T_2' mechanisms could include phase noise on the injection lock between the FORT and Raman lasers, or scattering due to stray light.

The exponential decay that damps Rabi oscillations is given by T_2. In order to separate out the components of T_2, we must turn to other techniques, such as Ramsey interferometry. Here one prepares the sample in an initial spin state, then applies a $\pi/2$ pulse with detuning Δ in order to rotate the spins into the x-y plane of the Bloch sphere picture (in a frame rotating at the frequency difference between the two spins). The spins precess in the plane with frequency Δ, so that if we apply a second $\pi/2$ pulse after a variable time t, we will observe Ramsey oscillations at frequency Δ. However, as the spins precess in the plane, they also drift out of phase with one another, so the oscillations that we measure will be exponentially damped at some rate. The point is that every measurement consists of two $\pi/2$ pulses separated by a time t, which is varied while the system is "in the dark" to applied fields. Thus, decoherence mechanisms that accumulate in Rabi oscillations as a function of pulse length (for example, scattering due to the applied fields) will be constant over the Ramsey data set and will only affect the amplitude of oscillations, not their rate of decay. Also, note that inhomogeneous mechanisms that cause a variation in Ω will not contribute, as long as the effective pulse lengths are reasonable approximations of $\pi/2$. Ramsey decoherence is the result of inhomogeneities in detuning from Raman

resonance, which cause different precession frequencies for each measurement.

Thus, Ramsey interferometry can give us information about a smaller subset of decoherence mechanisms on our experiment: those effects dependent on either magnetic field or temperature. Temperature-dependent decoherence may come as a surprise, given the statement above that finite atom temperature results in a spread of Rabi frequencies, to which Ramsey interferometry should be insensitive. However, atom temperature also produces a spread in detunings, given the FORT-induced differential AC-Stark shift in our experiment. Consider that the free-space hyperfine splitting Δ_{HF} between cesium ground states $F = 3$ and $F = 4$ is modified by 20 kHz at the bottom of each FORT well; halfway up the FORT well, the differential shift is only 10 kHz. Thus, as an atom moves within this potential, it experiences frequency shifts on the order of 10 kHz with respect to the frequency of the Raman pair. Depending on the Raman linewidth — that is, the Rabi frequency — this may be a significant effect.

Spin echo is a second diagnostic technique that we can apply to the problem of decoherence. Known as "photon echo" in the optical case, it allows us to recover some of the coherence lost to dephasing in Ramsey interferometry. Here we follow the Ramsey scheme above, using a fixed precession time t in the x-y plane, except that now we insert a π pulse at time $t/2$. This flips each precessing spin with respect to the x axis, so that the "fast" spins now lag behind the "slow" ones. After another $t/2$ interval, all the spins are back in phase, and the second $\pi/2$ pulse should rotate them to the Bloch sphere pole opposite where they began. However, rephasing only occurs for coherent decay mechanisms that are constant over t, so that the second $t/2$ interval "undoes" the first. Thus, any damping of photon echo amplitude as a function of time allows us to characterize T_2' as well as rapidly varying T_2^* mechanisms, such as fast magnetic field fluctuations.

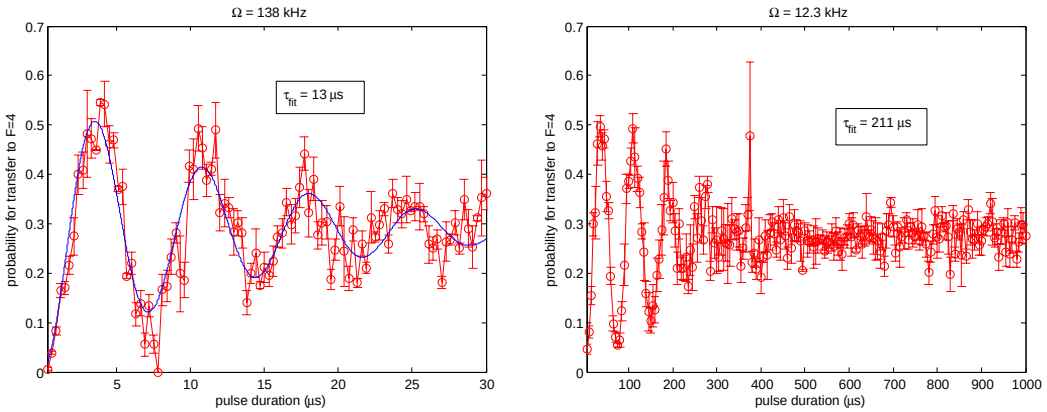

Figure 5.2: Rabi flops on the $|3,0\rangle \leftrightarrow |4,0\rangle$ resonance at $\Omega = 138$ kHz and $\Omega = 12.3$ kHz. For each measurement, atoms are prepared with roughly 60% efficiency in $|3,0\rangle$, then driven with a Raman pulse of varying duration, followed by state detection.

5.2.2 Rabi flopping measurements

Given the that our FORT and Raman beams are linearly polarized, mutually orthogonal, and propagate along the cavity axis, we can drive Raman transitions between pairs of Zeeman states with Rabi frequency Ω_E:

$$\langle 4,m|\hat{\Omega}_E|3,m\rangle = \sqrt{1-m^2/16}\;\Omega_0\cos\theta \tag{5.6}$$

$$\langle 4,m+1|\hat{\Omega}_E|3,m\rangle = -\frac{1}{8}\sqrt{(4+m)(5+m)}\;\Omega_0\sin\theta \tag{5.7}$$

where Ω_0 is the Rabi frequency for the $m = 0$ pair and θ is the angle between the cavity axis and the quantization axis, which we define along the applied magnetic field [19]. We see that Ω_E is m-dependent, so that in order to observe single-frequency oscillations, we will need to apply a magnetic bias field so that we can address only one pair at a time. A quantization axis along the cavity axis ($\theta = 0$) will allow $\Delta m = 0$ transitions while suppressing $\Delta m = \pm 1$. For high-contrast oscillations, we must be able to prepare atoms in a given initial Zeeman state; atoms prepared in the wrong state will not be addressed by the Raman frequency, so they will not contribute to decoherence, but they will result in a reduced amplitude.

The first demonstrations of Rabi flopping in our lab used conventional optical

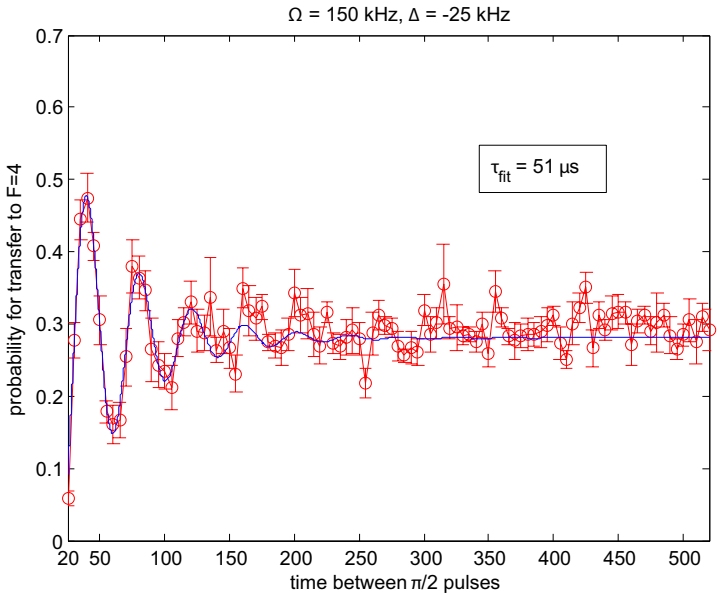

Figure 5.3: Ramsey interferometry at $\Omega = 150$ kHz, with detuning $\Delta = -25$ kHz from the $|3,0\rangle \leftrightarrow |4,0\rangle$ transition. Atoms are prepared in $|3,0\rangle$, then driven with a pair of $\pi/2$ pulses separated by a variable time t, followed by state detection. The number of coherent oscillations is roughly the same as for Rabi flopping measurements (Figure 5.2).

pumping techniques to prepare atoms in $|F = 3, m_F = 0\rangle$ [19], but we now rely on the method presented in Section 4.1; one advantage is that this allows us to compare the field-insensitive $|3,0\rangle \leftrightarrow |4,0\rangle$ transition with the other six field-dependent transitions. After conditional loading and optical pumping, we are left with a single atom in a given $F = 3$ sublevel. We drive Raman transitions at a fixed Rabi frequency for a variable time t, then perform state detection to determine the probability of transfer to $F = 4$ [30]. Sample Rabi flopping traces on $|3,0\rangle \leftrightarrow |4,0\rangle$, accumulated over a series of atoms, are shown in Figure 5.2.

We emphasize two observed features of field-insensitive Rabi flops in our experiment that provide insight into the decoherence mechanisms at work. First, we find that T_2 decay times are inversely proportional to Rabi frequency Ω. Thus, independent of Ω, an atom driven on resonance undergoes the same number of coherent flops (about three) before decoherence takes over. This effect can be seen in Figure 5.2, where the traces shown appear qualitatively similar despite the order of magnitude

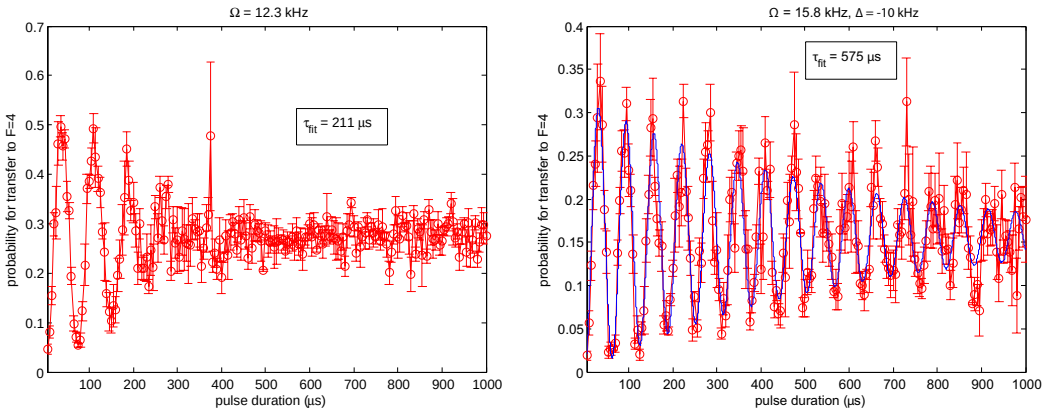

Figure 5.4: Two Rabi flopping measurements at similar Rabi frequencies, one on resonance and the other red-detuned by $\Delta = -10$ kHz. The on-resonance data is reproduced from Figure 5.2 for comparison; note that detuning to the red increases the damping time constant by almost a factor of three.

difference in Ω. Furthermore, Ramsey interferometry (Figure 5.3) does not extend the number of coherent oscillations, so we can rule out mechanisms to which Ramsey methods are insensitive, such as variation in Raman intensity and phase noise on the injection lock. We conclude that temperature effects are probably the cause of dephasing. Atoms with a finite temperature are not localized at the FORT minima; because of the spatial dependence of Ω, our flopping measurement occurs over an ensemble of atoms with a range of Rabi frequencies, and the measured ratio of T_2 to t_π tells us about this range.

A second, more perplexing finding is that by detuning the Raman pair to the red of resonance (negative Δ), we are able to improve coherence times. This is shown in Figure 5.4 for the case $\Delta = -25$ kHz at a Rabi frequency of 150 kHz, parameters for which we have observed the most significant improvement. In contrast, detuning the Raman pair to the blue side of resonance (positive Δ) somewhat degrades the coherence, though this is not as strong an effect. We now believe that this detuning dependence is due to the FORT-induced differential AC-Stark shift described in Section 5.2.1. Depending on an atom's temperature and thus location in the FORT potential, it may be in or out of resonance with the Rabi frequency of the Raman pair; due to the AC-Stark shift, the detuning Δ is spatially dependent. By detuning to the

red, we shift the Raman pair out of resonance with all atoms, so that only the coldest atoms will see an appreciable field; in this way, we are narrowing the distribution of Rabi frequencies in our experiment. David Boozer has written computer simulations that include this AC-Stark shift effect, and we find that they are in good agreement with our data.

Finally, one may ask if there are additional limits placed on T_2 in the case of field-sensitive ($m \neq 0$) transitions. Preliminary evidence suggests that this may be the case. However, with Rabi flopping measurements, it is difficult to distinguish between fast magnetic field drifts (on the timescale of decoherence for each atom) and slow drifts (on the timescale of the measurement over the ensemble). Based on sequential Raman spectrum measurements of the $|3,1\rangle \leftrightarrow |4,1\rangle$ transition, we have evidence for drifts of $\sim$ 10 kHz in the course of an hour. We have demonstrated spin echo for the $m = 0$ transition (Figure 5.5), but it would be interesting to apply this technique in the field-sensitive case: as photon echo should be insensitive to slow field drifts, a measurement of pulse amplitude as a function of precession time would provide information about fast fluctuations.

While Rabi flopping measurements have helped us to understand the limitations of our experiment, they also provide more direct insight on the prospects for atom-photon entanglement. We have seen that there is minimal decoherence over the course of a single π pulse, which is encouraging. However, in the case of π pulses on the $|3,0\rangle \leftrightarrow |4,\pm 1\rangle$ transitions, magnetic field drifts are a cause for concern. We should expect to use Rabi frequencies much faster than the $\sim$ 10 kHz drift range so that the transitions do not shift out of resonance in the course of the experiment. As we will see in the following sections, this imposes a severe restriction if we would like to replace optical Raman processes by driving ground state transitions directly with microwaves.

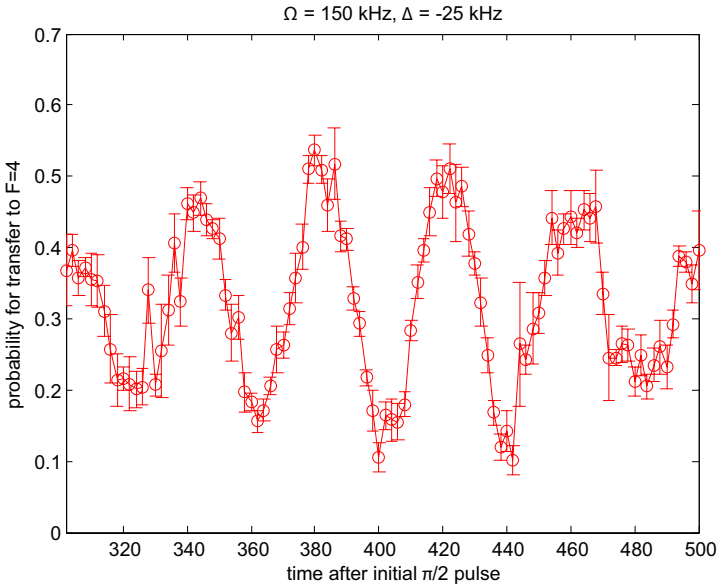

Figure 5.5: Spin echo measurement at $\Omega = 150$ kHz, with detuning $\Delta = 25$ kHz from the $|3,0\rangle \leftrightarrow |4,0\rangle$ transition. Atoms are prepared in $|3,0\rangle$, then driven with a $\pi/2$ pulse at time $t = 0$, a π pulse at $t = 200$ μs, and a second $\pi/2$ pulse at variable time t between 300 and 500 μs. The pulse sequence is followed by state detection. Note the revival of the Ramsey oscillations of Figure 5.3, with no observed reduction in amplitude.

5.3 Zeeman to hyperfine mapping

A significant challenge in demonstrating the proposed mapping from Zeeman to hyperfine states has been to implement $\Delta m = \pm 1$ transitions in our experiment. We have attempted this using various methods, each of which has presented its own set of drawbacks. We have been most successful in driving Raman transitions in the presence of a magnetic field transverse to the cavity axis, as well as in preliminary efforts with microwaves. I begin, however, with a discussion of our earlier attempts, which may provide some insight into the technical limitations of our experiment.

5.3.1 936 nm Raman transitions from the side of the cavity

In the presence of a bias field along the cavity axis, our current FORT-Raman configuration only drives $\Delta m = 0$ transitions. One means of accessing $\Delta m = \pm 1$ transitions is to replace the Raman beam with a beam from the side of the cavity at the same fre-

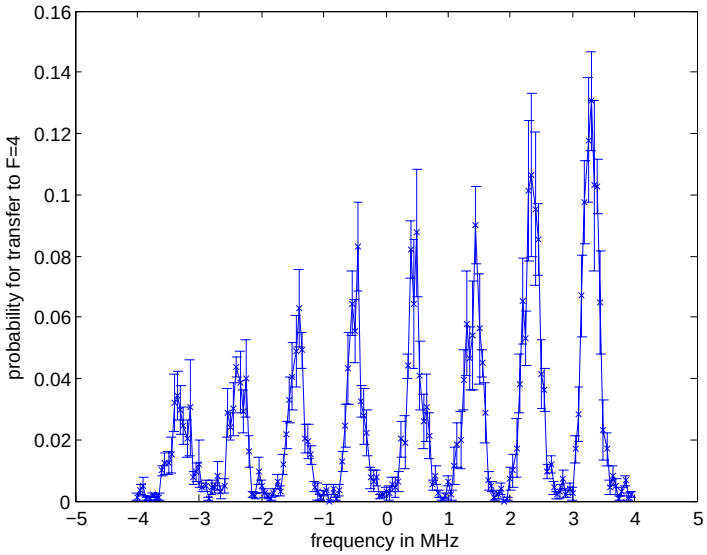

Figure 5.6: We replace the on-axis Raman beam with a 936 nm beam from the side of the cavity in order to drive $\Delta m = \pm 1$ transitions. We apply a magnetic field along the cavity axis and prepare atoms in $F = 3$, then measure the probability to transfer population to $F = 4$ after 150 μs Raman pulses, as a function of Raman detuning. The Raman spectrum now consists of eight possible m-changing frequencies: six degenerate pairs and two edge transitions.

quency, but polarized along the cavity axis; in this case, the vector orthogonal to the FORT-Raman polarization is also orthogonal to the quantization axis, and $\theta = \pi/2$ in equations (5.6) and (5.7). We have successfully demonstrated Raman transitions in this configuration (Figure 5.6). Note that a Raman spectrum consists of eight possible m-changing frequencies, interleaved between the seven $\Delta m = 0$ transition frequencies. Six of the frequencies correspond to pairs of transitions: $|3, m\rangle \rightarrow |4, m+1\rangle$ and $|3, m+1\rangle \rightarrow |4, m\rangle$ are degenerate for $m = \{-3, -2, ...1, 2\}$. The two edge transitions $|3, 3\rangle \rightarrow |4, 4\rangle$ and $|3, -3\rangle \rightarrow |4, -4\rangle$ are nondegenerate.

Unfortunately, we encountered two problems driving transitions in this configuration: first, we were limited by the power available in our Raman diode laser. With 2.2 mW of power focused from the side of the cavity, we found that it took about 150 μs to transfer population between the hyperfine ground states. Second and more problematic was the fact that we were unable to observe Rabi flops between $F = 3$ and $F = 4$ after preparation in $m_F = 0$; the population as a function of time simply

began in one state and ended in the other, just as for the incoherent Raman transfer of Figure 4.7. We now believe that this is likely due to diffraction of the Raman side beam by the cavity mirrors, which results in significant intensity variation over the possible FORT wells. This means that each well has a different rate for population transfer, and we would not be able to set a well-defined π pulse time in our experiments.

5.3.2 852 nm Raman transitions from the side of the cavity

At the time, we did not yet appreciate the role of diffraction in driving transitions from the side of the cavity. We believed that our failure to observe Rabi flops was due to the slow time for population transfer between ground states, during which decoherence mechanisms might play a significant role. In search of less stringent power requirements and faster Raman transitions, we switched to a pair of Raman lasers at 852 nm, detuned 3 GHz to the red of the cesium $D2$ resonances. The new lasers were set up in an adjoining lab (the former lab 1 cavity QED experiment, now relocated to lab 9); as in our 936 nm Raman pair, a 9.2 GHz frequency sideband applied to one laser was used to injection-lock the second. We monitored this injection lock by combining light from both lasers on a fiber beamsplitter with a laser locked to the cesium resonance and monitoring the optical beat note on a spectrum analyzer. The light from the Raman pair was brought to the cavity via optical fiber and focused in through the side.

We were again unable to observe Rabi flopping on individual Zeeman transitions. In retrospect, of course, this method suffers from the same side-beam diffraction problems as the previous 936 nm Raman attempt. However, we were able to observe incoherent $\Delta m = \pm 1$ Raman spectra using 10 μs pulses, an order of magnitude faster than with the 936 nm Raman pair.

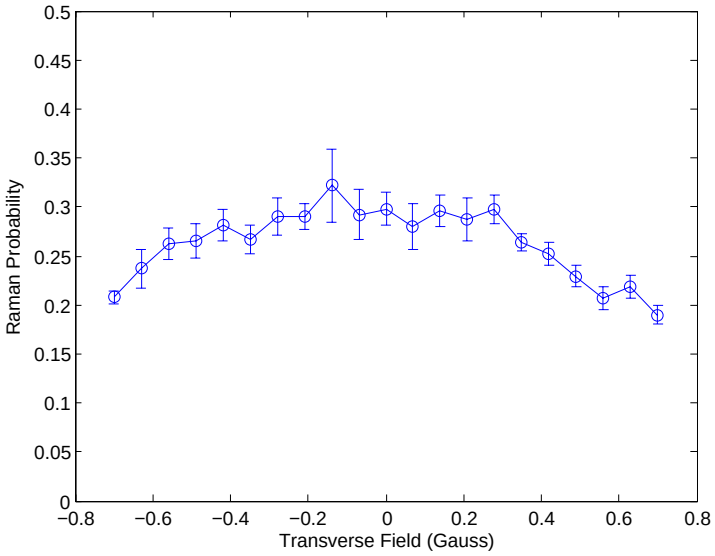

Figure 5.7: We measure the probability to optically pump into the state $|3,0\rangle$ as a function of a transverse magnetic field applied in addition to a constant axial field of 1.21 Gauss. The transfer probability to $F = 4$ after optical pumping is measured using incoherent Raman transitions, with a maximum possible value of 0.5.

5.3.3 Raman transitions using a transverse field

A third scheme for driving $\Delta m = \pm 1$ transitions relies on our original FORT-Raman pair, but requires us to apply a small transverse magnetic field on top of the axial field already present. We see from equation (5.7) that for small θ, the Rabi frequency for $\Delta m = \pm 1$ transitions is small, but as we increase θ, we will be able to drive m-changing transitions more rapidly. On the other hand, a nonzero θ means that the quantization axis and the cavity axis are no longer the same; specifically, the polarization modes supported by the cavity do not correspond exactly to decay from $|5',0\rangle$ to $|4,\pm 1\rangle$ as in Figure 5.1, and there is now some $|4,0\rangle$ component. By keeping the transverse field small with respect to the axial field, we hope to minimize this effect.

Our initial concern was that with the addition of the transverse field, the effectiveness of our optical pumping to $|3,0\rangle$ would be reduced because of mixing between states. However, measurements of population prepared in $|3,0\rangle$ as a function of field strength showed that this was a small effect, significant only for strong transverse fields

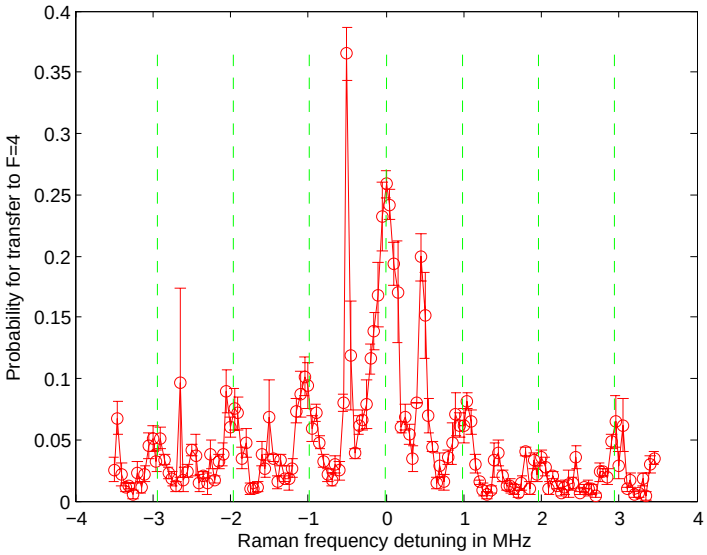

Figure 5.8: We prepare atoms in $|3,0\rangle$ and measure a Raman spectrum as in Figure 4.6, but in the presence of an 0.52 Gauss transverse field on top of a 1.21 Gauss axial field. Spaced between the $\Delta m = 0$ transitions indicated by dashed vertical lines, we see $\Delta m = \pm 1$ transitions, most prominently from $|3,0\rangle$ to $|4,\pm 1\rangle$. As the Rabi frequencies are lower for these transitions (equation (5.7)), the Raman pulse time is not long enough for decoherence to occur, so the measured transition probabilities have not yet reached their asymptotic values.

(Figure 5.7). We then measured Raman spectra in the presence of a 0.5 Gauss transverse field after optical pumping to identify transition frequencies for $|3,0\rangle \rightarrow |4,\pm 1\rangle$ (Figure 5.8).[1] We have confirmed that we can drive Rabi flops on these frequencies, both individually and jointly (Figure 5.9). In the case where both $|3,0\rangle \rightarrow |4,1\rangle$ and $|3,0\rangle \rightarrow |4,-1\rangle$ transitions are driven simultaneously, we expect the effective Rabi frequency to increase by a factor of $\sqrt{2}$.

We have investigated our ability to map a superposition state of $|4,\pm 1\rangle$ onto the hyperfine manifolds $F = 3$ and $F = 4$ in the following manner: we prepare an atom in $|3,0\rangle$, then drive it with two simultaneous π pulses on the $|3,0\rangle \rightarrow |4,1\rangle$ and $|3,0\rangle \rightarrow |4,-1\rangle$ transitions. (We thus prepare a superposition state analogous to the

[1] This transverse field is almost half the size of the axial field and thus larger than we would use for entanglement purposes. However, it allows us to drive Rabi flops quickly, and the superposition state mapping described below is not sensitive to the angle between the quantization and cavity axes.

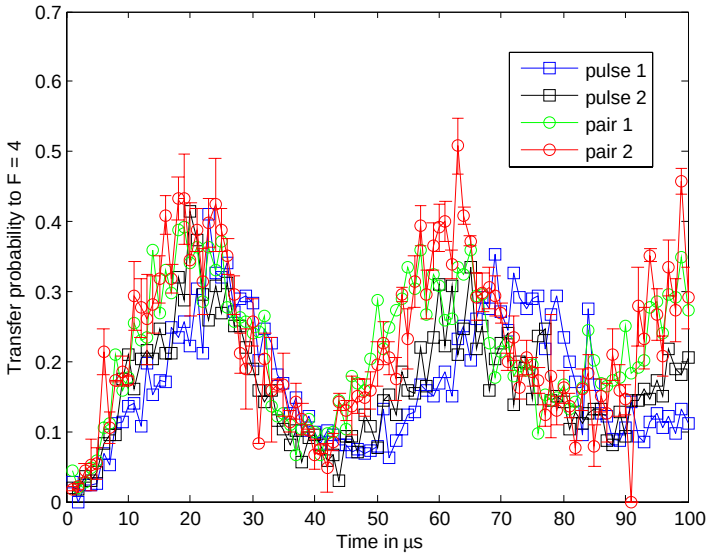

Figure 5.9: Individual and paired Rabi flops on the $|3,0\rangle \rightarrow |4,\pm 1\rangle$ transitions. We drive atoms prepared in $|3,0\rangle$ at the $\Delta m = +1$ and -1 transition frequencies for a variable time t, followed by state detection ($\Box$, blue and black). We then apply both frequencies simultaneously ($\circ$, green and red), where for testing purposes, the two pairs use different signal generators for the $|3,0\rangle \rightarrow |4,1\rangle$ transition. Note the increase in Rabi frequency by approximately $\sqrt{2}$ for the paired flops.

one we intend to create via decay from $|5',0\rangle$.) A second pair of π pulses attempts to map the superposition back to $|3,0\rangle$. Here we vary the phase of the $|3,0\rangle \rightarrow |4,1\rangle$ arm while holding the phase of the other arm constant; we expect the mapping processes in the two arms to interfere constructively or destructively as a function of phase. The result, shown in Figure 5.10, is a fringe with $\sim 75\%$ visibility. For comparison, we have also plotted the data from the same measurement sequence, but with the relative phase held constant.

The fringe visibility in Figure 5.10 is limited by our ability to prepare atoms in $|3,0\rangle$ and to drive coherent Raman π pulses between Zeeman pairs. We have some evidence that the off-axis magnetic field (and subsequent mixing between Zeeman states) interferes with these processes; namely, repeating the experiment above in the presence of a pure transverse field produces a fringe with significantly improved contrast. However, the presence of an axial field is necessary for the correspondence between photon polarization and Zeeman state that is the basis for our entanglement

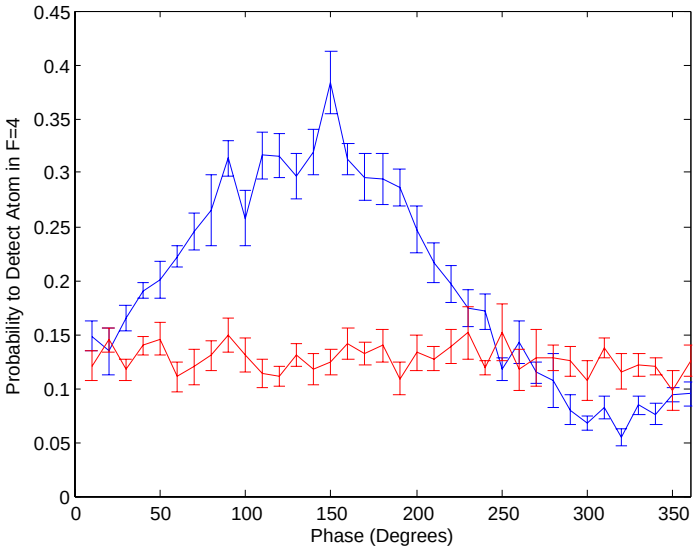

Figure 5.10: We prepare a superposition of Zeeman states $|4,1\rangle$ and $|4,-1\rangle$, then demonstrate a coherent mapping of this superposition to the hyperfine manifolds $F = 3$ and $F = 4$. We apply simultaneous π pulses on the $|3,0\rangle \rightarrow |4,1\rangle$ and $|3,0\rangle \rightarrow |4,-1\rangle$ transitions in order to transfer population to the $F = 3$ manifold, followed by state detection. Shown is the probability to detect an atom in $F = 4$ as a function of the relative phase between the two arms; for the red data, the experiment is repeated with the phase fixed at a random value. The data are plotted twice side by side to demonstrate the 2π periodicity.

scheme.

5.3.4 Microwave transitions

A final possibility is to forego optical Raman processes and drive $\Delta m = \pm 1$ transitions directly with microwaves at 9.2 GHz. By using microwaves, we avoid the problems resulting from spatial variation in Rabi frequency within each FORT well: the power from a microwave horn is constant across the μm-scale dimensions of the cavity, and every atom experiences the same Rabi frequency. (Atoms may still be shifted out of resonance with the microwaves as they move within the FORT, a result of the differential AC-Stark shift discussed in Section 5.2.)

While microwave horns are standard equipment in many atomic physics labs, they have not been used in our group prior to this experiment. An Agilent E8247C signal

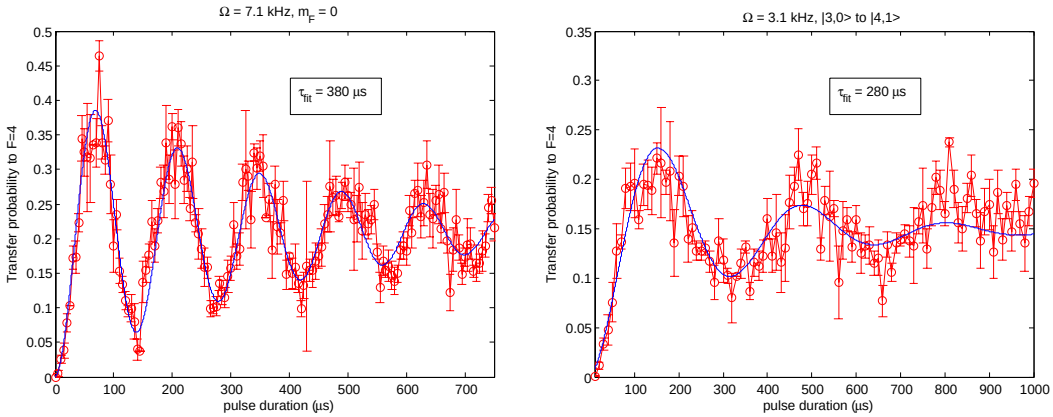

Figure 5.11: We drive microwave transitions directly between hyperfine ground states of cesium. Shown are Rabi flops on the $|3,0\rangle \rightarrow |4,0\rangle$ and $|3,0\rangle \rightarrow |4,1\rangle$ transitions.

generator provides us with a stable, RS-232-controlled microwave source. At the signal generator output is a microwave switch, followed by an amplifier. Between the amplifier and the microwave horn facing our cavity, we use a three-port circulator and a stub tuner in order to impedance-match the signal: we monitor the power in the reflected port of the circulator and adjust the stub tuner length to mimimize this value. The stub tuner was a helpful recommendation from Sabrina Leslie in the Stamper-Kurn group at Berkeley, who also suggested the use of Huber-Suhner cables to minimize signal loss.

Using the microwave horn, we have observed Rabi flops on the $|3,0\rangle \rightarrow |4,0\rangle$ and $|3,0\rangle \rightarrow |4,1\rangle$ transitions (Figure 5.11). We now have a new means to drive coherent transitions between hyperfine ground states, allowing us to access both $\Delta m = 0$ and $\Delta m = \pm 1$ transitions while avoiding the problems of a bias field at an angle to the quantization axis (Section 5.3.3). The challenge of driving microwave transitions in our experiment stems from the available power. The Rabi frequencies in Figure 5.11 are only 7 kHz, limited at present by the 3 W amplifier in the signal path. We do have a second, 20 W amplifier, but we would like to test cavity heating effects at this power before putting it to use. However, since the Rabi frequency only scales as the square root of power, we expect less than a factor of three improvement from this amplifier.

A narrow Rabi frequency means that the experiment is highly sensitive to shifts in detuning, whether as a result of motion in the FORT potential or changing magnetic fields. Moreover, the corresponding long π pulse times ($\sim 100\mu$s) place strict limits on acceptable decoherence rates. We have only recently begun to explore microwaves in a cavity QED setting, and there are certainly exciting applications ahead, but there are important issues that we will need to address in the process.

5.4 Fast pulses from the side of the cavity

We now have the means to map a Zeeman superposition onto a hyperfine superposition that we can measure. Here we return to the initial step in our entanglement protocol: using fast optical pulses from the side of the cavity to generate the Zeeman superposition along with a polarization-entangled photon. We discuss the implementation of these pulses in the lab and present correlation measurements between photon polarization and Zeeman state.

As in Figure 5.1, we would like to excite each atom from $|4,0\rangle$ to $|5',0\rangle$. We need to drive this transition with linearly polarized light along the cavity axis, so the pulse must come from the side of the cavity. From $|5',0\rangle$, the atom will decay into the cavity mode via a σ^+ or σ^- photon, and the photon polarization will be entangled with the atom's final ground state. Ideally, to prepare the atom in $F'=5$ after each pulse, the pulse length should be short with respect to $(2\gamma)^{-1} = 31$ ns and $2\pi(2g)^{-1} = 14.7$ ns. In practice, we are able to make pulses as short as 10 ns. Here we use $F = 4 \rightarrow F' = 5$ light from our master (probe) laser that is fiber-coupled into an amplitude modulator from EOSPACE Inc., a two-port Mach-Zehnder interferometer with a nominal 10 GHz bandwidth. We drive pulses with TTL signals to the modulator; additionally, we provide the modulator with a stable DC voltage V_π, which we adjust so as to maximize transmission when the TTL value is high. The measured suppression of the modulator is only 20 dB, so we enclose the fast modulator pulse within a slower AOM pulse applied to the light before the fiber input. Both pulses are driven from an SRS DG535 pulse generator triggered by the ADwin system. We use a Thorlabs

PDA10A 150 MHz detector to characterize the pulse shape at the cavity input.

We can make an estimate of the efficiency with which we expect these fast pulses to generate photons in the cavity mode. We first prepare atoms in $|3,0\rangle$ with optical pumping efficiency p_{pump}, where we have measured $p_{pump} \approx 0.6$. We then drive a π pulse from $|3,0\rangle \rightarrow |4,0\rangle$, where we estimate $p_\pi \approx 0.8$ based on Rabi flopping data. After attempting to prepare the atom in $|4,0\rangle$, we apply a single pulse from the side of the cavity on the $|4,0\rangle \rightarrow |5',0\rangle$ transition. The pulse cycles population rapidly between the ground and excited states of the atom, so that the probability for the atom to be in $|5',0\rangle$ at the end of the pulse is $p_{excite} = 0.5$. Meanwhile, an atom in $|5',0\rangle$ will decay with probability $p_{decay} = 0.59$ into the cavity mode and the rest of the time into free space.[2] We thus expect

$$p_{photon} = p_{pump} \times p_\pi \times p_{excite} \times p_{decay} \tag{5.8}$$

$$= 0.6 \times 0.8 \times 0.5 \times 0.59 \tag{5.9}$$

$$= 0.14. \tag{5.10}$$

In order to estimate the rate of photon detection at our SPCMs, we need to include the measured path efficiency $p_{path} = 0.024$ [16]; $p_{photon} \times p_{path} = 0.0034$. This is in reasonable agreement with the photon detection rate of 0.0046 that we have measured in the lab.

Our next step was to measure correlations between the detection of a cavity photon and the final Zeeman state of an atom. After the sequence above (state preparation, π pulse from $|3,0\rangle \rightarrow |4,0\rangle$, fast pulse from the side), we introduced a state-detection measurement, preceded by either zero, one, or two Zeeman-specific π pulses. In the absence of any π pulses, state detection conditioned on the detection of a cavity

[2] A simple way to understand this is to remember that the atomic excited state is a superposition of the two atom-cavity eigenstates. The system will thus oscillate at rate $2g$ between having one excitation in the atom and one excitation in the cavity. When the excitation is in the atom, decay is possible at rate γ into free space (as the cavity mode subtends only a small fraction of the 4π solid angle); when the excitation is in the cavity, decay takes place at rate κ into the cavity output mode. Assuming that $g \gg \kappa, \gamma$, the atom spends about half the time in each state, and the probabilities for decay via the atom and cavity channels are $\frac{\gamma}{\kappa+\gamma}$ and $\frac{\kappa}{\kappa+\gamma}$, respectively.

output photon should confirm that the atom is in $F = 4$, since the only decay channel from $F' = 5$ is to $F = 4$. Of course, we expect atoms not only to be in $F = 4$, but more specifically, to be in one of the two Zeeman levels $|4, 1\rangle$ and $|4, -1\rangle$. We can evaluate the population in a given Zeeman level by selectively depopulating that level with a π pulse before the state detection process. For example, if we insert a π pulse from $|4, 0\rangle \rightarrow |3, 0\rangle$ before state detection, we still expect to find all atoms in $F = 4$ afterwards (conditioned on a photon), since we do not expect decay into the cavity mode from $F' = 5$ to $|4, 0\rangle$. In contrast, we expect that a π pulse from $|4, 1\rangle \rightarrow |3, 1\rangle$ or $|4, -1\rangle \rightarrow |3, -1\rangle$ would reduce the probability to detect population in $F = 4$ by half.

Note that the uncorrelated data in this experiment is also a source of interesting information. In the absence of π pulses, the unconditional probability to detect a photon in $F = 4$ reflects our ability to prepare an atom in $|4, 0\rangle$. (Here we assume that every atom not optically pumped to $|3, 0\rangle$ is prepared in another Zeeman state of the $F = 3$ manifold, and that our π pulse only addresses the $|3, 0\rangle$ state.) Moreover, the unconditional π pulse data tells us about the atomic decay into both the cavity mode and free space. Recall that while we expect the atom to decay via the cavity mode 59% of the time (into $|4, 1\rangle$ and $|4, -1\rangle$, with equal probability), it also decays 41% of the time into free space, where the branching ratios of the cesium transitions determine the final Zeeman states. Specifically, in the case of free space decay, we expect the atom to decay to $|4, 0\rangle$ with probability $p_{fs0} = 0.55$ and to $|4, 1\rangle$ and $|4, -1\rangle$ with probabilities $p_{fs1} = p_{fs-1} = 0.22$. In the uncorrelated case, we also need to remember that the atom is left unexcited in $|4, 0\rangle$ after half of all pulses. When we include this fact and weight the Zeeman state probabilities of the two decay channels, we find the expected probabilities

$$p_1 = p_{-1} = 0.5(0.41 \times 0.22 + 0.59 \times 0.5) = 0.19; \tag{5.11}$$

$$p_0 = 0.5 + 0.5(0.41 \times 0.55) = 0.61. \tag{5.12}$$

A more thorough calculation also takes into account the imperfect nature of our state

π pulse(s)	P_4, unconditional	P_4, conditional
none	0.62	0.92
$\|4,0\rangle \rightarrow \|3,0\rangle$	0.33	0.84
$\|4,1\rangle \rightarrow \|3,1\rangle$	0.57	0.70
$\|4,-1\rangle \rightarrow \|3,-1\rangle$	0.56	0.62
$\|4,1\rangle \rightarrow \|3,1\rangle$ and $\|4,-1\rangle \rightarrow \|3,-1\rangle$	0.53	0.35

Table 5.1: Measured correlations between a detected cavity photon and the Zeeman state of a trapped atom. We attempt to prepare each atom in $|4,0\rangle$ and excite it to $|5',0\rangle$ with a short pulse from the side of the cavity. We then measure the probability P_4 that the atom is in $F = 4$ following zero, one, or two Zeeman-specific π pulses; this is expressed both as an unconditional probability and conditioned on the detection of a photon in the cavity output path.

preparation and π pulses; in this case, we have

$$p'_1 = p'_{-1} = p_{pump} \times p_\pi \times 0.5(0.41 \times 0.22 + 0.59 \times 0.5) - 0.1 \times p_\pi = 0.01, \quad (5.13)$$

$$p'_0 = 0.8 \times (0.5 + 0.5(0.41 \times 0.55)) - 0.1 \times p_\pi = 0.21, \quad (5.14)$$

where the additional term reflects the fact that atomic population left in $F = 3$ after the initial π pulse (roughly 10% for each of the three Zeeman manifolds) can be brought into the $F = 4$ manifold by the second, diagnostic pulse.

The results of our measurements are summarized in Table 5.1. After state preparation and excitation to $|5',0\rangle$, the unconditional probability to find an atom in the $F = 4$ manifold is 0.62, somewhat better than our optical pumping and π pulse estimates, and the conditional probability is 0.92. The fact that this value is not 1 can be interpreted as the result of background photon counts that occur during the 38% of all trials when the atom is not successfully prepared in $F = 4$.

Following a π pulse from $|4,0\rangle \rightarrow |3,0\rangle$, the unconditional probability to detect an atom drops to 0.33 and the conditional probability to 0.84. From p'_0 and the probability to find an atom in $F = 4$, we would anticipate the unconditional probability to be $0.62 - 0.21 = 0.41$. The conditional probability can again be understood in terms of background photon counts: as the unconditional probability to find an atom in $F = 3$ is two times greater than without the π pulse, the chance that background

counts (interpreted as cavity photons) will coincide with an atom in $F = 3$ is also two times greater, and the conditional $F = 3$ probability doubles from 0.08 to 0.16.

The unconditional probabilities following π pulses from $|4, 1\rangle \rightarrow |3, 1\rangle$ and $|4, -1\rangle \rightarrow |3, -1\rangle$ are 0.57 and 0.56, respectively. In comparison, we would expect values of $0.62 - p_1' = 0.61$ in both cases. (Again, the discrepancy suggests that for this data run, our optical pumping efficiency was better than usual.) The conditional probabilities measured are 0.62 and 0.70. We would expect to measure roughly

$$p_{c1} = p_{c-1} = 0.90 \times (1 - 0.5 \times 0.8 + 0.1 \times 0.8) = 0.61, \tag{5.15}$$

where the second term expresses the depopulation of the Zeeman level (to which the atom has decayed with probability 0.5) by an imperfect π pulse, the third term is the probability that population in $|3, 1\rangle$ or $|3, -1\rangle$ will be excited to $F = 4$ by this π pulse, and the overall scaling reflects background photon counts as above. Thus, we find good agreement between the data and our model; we do not yet have a good explanation for the asymmetry in the two conditional probabilities, but it may be connected with the cavity birefringence.

Finally, we apply a pair of π pulses on both $|4, \pm 1\rangle \rightarrow |3, \pm 1\rangle$ in sequence before state detection; in this case, we find unconditional and conditional probabilities of 0.53 and 0.35. Here we expect an unconditional value of $0.62 - 2 \times p_1' = 0.60$ and a conditional value of

$$p_{c\pm1} = 0.90 \times (1 - 2(0.5 \times 0.8 + 0.1 \times 0.8)) = 0.32, \tag{5.16}$$

again consistent with the data.

We have thus observed correlations between between photons generated via fast pulses from the side of the cavity and atoms prepared in $|4, \pm 1\rangle$. In the near future, we hope to combine these correlation measurements with the hyperfine mapping of Section 5.3. After applying a fast pulse from the side of the cavity at $t = 0$, we would attempt to transfer the Zeeman populations in $|4, \pm 1\rangle$ to $F = 3$, followed by state

detection. Conditioned on the detection of a photon at the cavity output, we expect that the hyperfine population measurement would result in a fringe as a function of t, due to precession of the Zeeman superposition state. We could then consider the long-anticipated rebuild of our cavity output path: while we are now only able to detect one photon output polarization, the ability to detect orthogonal polarizations in parallel would permit a Bell measurement of atom and photon states.